RESEARCH ARTICLE

Key Points:
- Highly elliptical orbit (HEO) satellites can improve high-latitude coverage
- We conduct flux inversions with simulated CO_2 from GOSAT and a HEO mission
- HEO offers major advantages for constraining Arctic and boreal CO_2 fluxes

Correspondence to:
R. Nassar,
ray.nassar@ec.gc.ca

Satellite observations of CO₂ from a highly elliptical orbit for studies of the Arctic and boreal carbon cycle

Ray Nassar[1], Chris E. Sioris[2], Dylan B. A. Jones[3], and John C. McConnell[2,4]

[1]Climate Research Division, Environment Canada, Toronto, Ontario, Canada, [2]Department of Earth and Space Science and Engineering, York University, Toronto, Ontario, Canada, [3]Department of Physics, University of Toronto, Toronto, Ontario, Canada, [4]Deceased 29 July 2013

Abstract Here we report on an observing system simulation experiment (OSSE) to compare the efficacy of near-infrared satellite observations of CO_2 from a highly elliptical orbit (HEO) and a low Earth orbit (LEO), for constraining Arctic and boreal CO_2 sources and sinks. The carbon cycle at these latitudes (~50–90°N) is primarily driven by the boreal forests, but increasing anthropogenic activity and the effects of climate change such as thawing of permafrost throughout this region could also have an important role in the coming years. A HEO enables quasi-geostationary observations of Earth's northern high latitudes, which are not observed from a geostationary orbit. The orbit and observing characteristics for the HEO mission are based on the Weather, Climate and Air quality (WCA) concept proposed for the Polar Communications and Weather (PCW) mission, while those for the LEO mission are based on the Greenhouse gases Observing Satellite (GOSAT). Two WCA instrument configurations were investigated. Adopting the *Optimal* configuration yielded an observation data set that gave annual Arctic and boreal regional terrestrial biospheric CO_2 flux uncertainties an average of 30% lower than those from GOSAT, while a smaller instrument configuration resulted in uncertainties averaging 20% lower than those from GOSAT. For either WCA instrument configuration, much greater reductions in uncertainty occur for spring, summer, and autumn than for winter, with *Optimal* flux uncertainties for June–August nearly 50% lower than from GOSAT. These findings demonstrate that CO_2 observations from HEO offer significant advantages over LEO for constraining CO_2 fluxes from the Arctic and boreal regions.

1. Introduction

An improved understanding of Earth's carbon cycle at global to regional scales is important for predicting future atmospheric greenhouse gas concentrations and thus making accurate projections of future climate. The Arctic and boreal latitudes (defined here as 50–90°N) play an important role in the global carbon cycle and have experienced the largest temperature increases in recent decades [*Hansen et al.*, 2010], a trend that is expected to continue. Research and monitoring of the carbon cycle of the north will therefore be especially important in a changing climate.

The primary driver of the carbon cycle at northern latitudes is the boreal forest (comprising 30% of the world's forest area). These forests, occurring poleward of approximately 50°N, have a particularly strong influence on the seasonal cycle of northern hemispheric atmospheric CO_2 [*Keeling*, 1960]. Climate change interacts with the carbon cycle of the boreal forests in several ways, for example, by lengthening the growing season [*McDonald et al.*, 2004], which could increase annual net CO_2 uptake [*Black et al.*, 2000]. Boreal forest disturbances, such as increased fire activity and insect infestations, have also become more common [*Stinson et al.*, 2011] as the climate has changed. These disturbances perturb the carbon cycle by causing major losses of living biomass carbon, some of which is released quickly to the atmosphere as CO_2, while some is converted to dead organic matter and released slowly as CO_2 in subsequent years. Such opposing carbon-climate feedbacks make the future carbon balance of the boreal forests difficult to predict.

Arctic sea ice extent and volume are declining rapidly, such that summers with virtually no sea ice are predicted to occur by the 2030s [*Wang and Overland*, 2012]. The impact of a seasonally ice-free Arctic Ocean on the CO_2 air-sea flux is not well understood, but could have consequences for the global carbon cycle [*Cai et al.*, 2010; *Halloran*, 2012]. Long before summer sea ice is totally absent, shipping across the Arctic Ocean is expected to increase [*Corbett et al.*, 2010], along with accelerated exploration and extraction of petroleum and other resources at high latitudes [*Peters et al.*, 2011], causing additional perturbations to the Arctic carbon cycle.

Increased photosynthetic uptake by Arctic and sub-Arctic tundra or "greening" in response to warming may already be occurring [*Oechel et al.*, 2000; *McGuire et al.*, 2009; *Xu et al.*, 2013], but the magnitude of this phenomenon and its impact on the future net carbon balance of the Arctic are highly uncertain. The carbon content of Northern Hemisphere permafrost is estimated at 1672 PgC [*Tarnocai et al.*, 2009], which is twice the total amount of carbon presently in the atmosphere (~835 PgC). Permafrost spans an area of ~18.8 million km^2 and as these frozen, carbon-containing soils warm, some carbon from the uppermost layers can be released to the atmosphere. A fraction will be released as CH_4 under the anaerobic (oxygen limited) conditions found in wetland areas, lowlands, or valleys, but most carbon will be emitted as CO_2, especially under aerobic conditions found on dry, elevated, or sloped land [*Schuur et al.*, 2008]. The heterogeneity of permafrost and its changing conditions make the exact balance between CH_4 and CO_2 difficult to predict, yet this is important for understanding the potential for the permafrost carbon feedback with climate change. The potential for the rapid release of permafrost carbon to the atmosphere and the resulting feedback is controversial. Recent model simulations of the quantity and timing of permafrost carbon release for the remainder of the century span a wide range, from a low of ~9 PgC [*Schneider von Deimling et al.*, 2012], under a scenario that includes negative anthropogenic emissions (Representative Concentration Pathway 3 peak and decline) to a high of 104 ± 37 PgC [*Schaefer et al.*, 2011]. The lowest estimate implies a negligible impact on global climate, while the larger estimate is roughly equal to the 2000–2012 cumulative global emissions from fossil fuel combustion and cement manufacture (~106 PgC) and would cause a positive feedback with global climate change that has not been accounted for in the Intergovernmental Panel on Climate Change Fifth Assessment Report or earlier climate predictions.

With such large uncertainty in the stability of permafrost carbon and the severe consequences if a positive feedback and accelerated warming result, it would be prudent to monitor permafrost CO_2 and CH_4 emissions beginning with baseline measurements as soon as possible. Designing an observing strategy to detect and monitor important changes to the high-latitude carbon cycle with in situ methods requires a priori knowledge or assumptions about the changes and where they will occur. Coordinated measurement networks such as the Circumpolar Active Layer Monitoring Network [*Brown et al.*, 2000] and the Thermal State of Permafrost network [*Romanovsky et al.*, 2011] currently exist and their expansion and long term operation has been wisely recommended [*United Nations Environment Program*, 2012], but these networks do not monitor permafrost carbon emissions. The Carbon in Arctic Reservoirs Vulnerability Experiment (CARVE) [*Miller and Dinardo*, 2012] and the Arctic and Boreal Vulnerability Experiment (ABoVE) will consist of a combination of in situ and remote measurements, including the use of dedicated small aircraft in and around Alaska, to explore environmental changes including permafrost vulnerability and emissions. However, targeted measurements over other parts of the Arctic are still lacking. To complement the existing networks, campaigns, and other measurement efforts, a satellite-based approach to monitoring CO_2 and CH_4 emissions from permafrost would be extremely valuable and consistent with the recommendations of the *Snow, Water, Ice, and Permafrost in the Arctic* [2011] report, which call for Arctic countries and international organizations to maintain and support the development of remote sensing methods for observing the cryosphere.

Satellite observations of CO_2 are increasingly contributing to our understanding of the global carbon cycle, in most cases by utilization of these data with atmospheric transport modeling. Most early satellite observations of CO_2 measured thermal infrared (TIR) emission [*Chahine et al.*, 2005, 2008; *Crévoisier et al.*, 2009; *Kulawik et al.*, 2010, 2013], which gives peak sensitivity to mid/upper tropospheric CO_2 (~5 km or above) and thus a limited amount of information about surface sources/sinks [*Nassar et al.*, 2011]. Scanning Imaging Absorption Spectrometer for Atmospheric Cartography (SCIAMACHY) CO_2 was based on near-infrared (NIR) solar reflectance, giving a record of daytime CO_2 column-averaged dry air mole fraction (XCO_2) over land spanning 2002–2012 [e.g., *Schneising et al.*, 2011; *Reuter et al.*, 2011]. The Greenhouse Gases Observing Satellite (GOSAT) [*Yokota et al.*, 2009], launched in 2009, makes NIR solar reflectance observations of CO_2 and the O_2 A band for XCO_2 retrieval over land and low-latitude oceans [*Yoshida et al.*, 2011, 2013; *O'Dell et al.*, 2012; *Crisp et al.*, 2012], along with TIR CO_2 during both day and night. The Orbiting Carbon Observatory 2 (OCO-2) [*Crisp et al.*, 2004, 2012] is scheduled to launch in July 2014, while TanSat, MicroCarb, GOSAT-2, CarbonSat, and other CO_2 missions are planned or proposed for the future; however, all of these missions will use a low Earth orbit (LEO). Carbon observing missions in LEO are commonly Sun synchronous, in which the satellite passes over a given point on the Earth at a fixed time of day. If the satellite has the ability to observe a wide swath, like the proposed CarbonSat mission [*Bovensmann et al.*, 2010], then at high latitudes, two daily observing opportunities at a given point may be possible from consecutive orbits, but obtaining more temporal coverage requires multiple LEO satellites in a constellation [*Velazco et al.*, 2011].

A geostationary or geosynchronous orbit (GEO) provides an alternate observing approach and is commonly used for communications and operational meteorological satellites. The European Space Agency (ESA) Earth Explorer 2 candidate geostationary tropospheric pollution explorer (GeoTROPE) [*Burrows et al.*, 2004] proposed to make GEO measurements of atmospheric composition but was not selected. Some GEO missions of atmospheric composition are planned, including ESA's Sentinel 4, NASA's Tropospheric Emissions: Monitoring of Pollution (TEMPO) [*Chance et al.*, 2012] and Geostationary Coastal and Air Pollution Events (GEO-CAPE) [*Fishman et al.*, 2012], and Korea's Geostationary Environment Monitoring Spectrometer (GEMS) on the Multipurpose Geostationary Satellite [*Kim and the GEMS Team*, 2012]. Unfortunately, XCO_2 capability is presently not planned for these missions, although CH_4 is a target species for GEO-CAPE and the possibility of expanding certain GEO missions to include XCO_2 capability is informally being considered. Dedicated CO_2 and CH_4 GEO mission proposals have recently begun to emerge. GEO has the major advantage of offering continuous coverage over a select region of the Earth, but observations are typically limited to ~55°S–55°N, with difficulty viewing higher latitudes due to the large nadir viewing angles from an equatorial orbit. Thus, neither LEO nor GEO is especially well suited to provide observations for carbon cycle studies at northern high latitudes.

The World Meteorological Organization (WMO) Vision for a Global Observing System in 2025 [*World Meteorological Organization*, 2009] recommends the use of highly elliptical orbits (HEOs) for obtaining dense high-latitude observations. From a HEO, with the Earth at one focus of the ellipse, the distance between the satellite and Earth changes during orbital motion with the satellite moving quickly while close to the Earth and slowly while farther away, thus conserving angular momentum. Observing during the dwelling time around the farthest point from Earth (the apogee) enables continuous observations at northern high latitudes for a period of 6–8 h per orbit (depending on specific parameters of the HEO), yielding the capability for delivering quasi-geostationary observations of Earth's polar regions. Thus, HEO satellites would be a critical component in any future constellation of CO_2 satellites, providing spatial coverage not obtained by GEO and temporal coverage not obtained from LEO.

In this paper, we conduct atmospheric CO_2 source/sink inversions with simulated data to investigate the impact of CO_2 column measurements from a proposed Canadian HEO mission compared to a LEO mission with the capabilities of GOSAT. The inversion with the simulated data provides the first quantitative assessment of the impact of HEO observations on our ability to constrain Arctic and boreal CO_2 sources and sinks, demonstrating improvements relative to current LEO capabilities.

2. The PCW-Polar Highly Elliptical Orbital Science-WCA Concept

The Polar Communications and Weather (PCW) mission is currently under consideration by the Canadian government. It would consist of two satellites in a HEO configuration, and as the name suggests, the primary drivers of the mission would be Arctic meteorological observations and communications capability. The addition of a science instrument payload to PCW with the capability of measuring numerous atmospheric trace gas species is being considered under the Polar Highly Elliptical Orbit Science (PHEOS) program. The Weather, Climate and Air quality (WCA) concept is one possible payload that was investigated in Phase 0 and A studies that were completed in early 2012 [*McConnell et al.*, 2012]. The WCA instrument suite would consist of an infrared high-resolution Fourier transform spectrometer (FTS) and the Ultraviolet Visible Spectrometer (UVS) with a dispersive grating design. The FTS would be designed and built by ABB Inc. with heritage from the Atmospheric Chemistry Experiment (ACE)-FTS [*Bernath et al.*, 2005] and GOSAT Thermal And Near infrared Sensor for carbon Observation (TANSO)-FTS [*Kuze et al.*, 2009], but with a smaller mass and volume. The PHEOS-FTS would have two-dimensional imaging capability rather than single pixel detectors (as described in section 3.2), with the spectral bands and spectral resolution shown in Table 1. It should be noted that due to instrument mass constraints, the spectral region for the 2.0 micron strong CO_2 band used in GOSAT and OCO-2 is currently not included, although this spectral region has long been known to be useful for quantifying scattering due to cloud and aerosol [*Kuang et al.*, 2002]. The nominal mass, size, and power allocations for the complete PHEOS payload on PCW are 50 kg, $30 \times 30 \times 30$ cm^3, and 100 W. Design and testing of prototype instruments has shown that meeting these constraints is extremely difficult and most likely not possible with the full capabilities desired for the instrument suite, so three configurations have been proposed for consideration [*McConnell et al.*, 2012; *Lachance et al.*, 2012].

Table 1. Proposed FTS Spectral Bands and Resolution

FTS Band	Spectral Range (μm)	Spectral Range (cm^{-1})	Spectral Resolution (cm^{-1})
1	14.2–6.7	700–1,500	0.25
2	5.6–3.7	1,800–2,700	0.25
3a	1.67–1.66	5,990–6,010	0.25
3b	1.67–1.60	5,990–6,257	0.25
4	0.766–0.760	13,060–13,168	0.50

1. *Optimal configuration* includes both the UVS and FTS instruments, with an FTS aperture diameter of 15 cm, which determines the amount of light entering the instrument and influences the signal-to-noise ratio (SNR). All FTS spectral bands for CO_2 and other target species are included (Bands 1, 2, 3b, 4 and the UVS), yielding a mass of 82 kg and volume of 103,800 cm^3.

2. *All-band configuration* includes both the instruments with the FTS aperture reduced to 10 cm, decreasing the amount of incoming light and thus the SNR. All FTS spectral bands for CO_2 and other target species are included (Bands 1, 2, 3b, 4 and the UVS), resulting in a mass of 45 kg and volume of 35,128 cm^3. In this paper, we will often refer to this configuration as "Lite".

3. *Compliant configuration* does not include the UVS and would use a narrowed NIR band 3 for CH_4 but with no CO_2 capability and no O_2 *A* band (only Bands 1, 2 and 3a). It would use a 10 cm FTS aperture, resulting in a mass of 37 kg and volume of 25,184 cm^3.

A 25% mass contingency and 20% volume contingency have been included in the values stated above. All configurations meet the allocated 100 W power. The *Compliant* configuration meets all allocations while the *All-band* or Lite configuration slightly exceeds the size and the *Optimal* exceeds both mass and size. The proposed FTS spectral resolution for the main CO_2 band is 0.25 cm^{-1} (maximum optical path difference of ±2.0 cm) which is between the nominal resolutions of GOSAT (0.20 cm^{-1}) and OCO−2 (~0.30 cm^{-1}). The proposed FTS ground pixel size is 10×10 km^2. Spectral resolution could be degraded to reduce instrument mass/volume, but this is not recommended due to the reduced measurement quality that would result from limitations on the ability to properly fit lineshapes of CO_2 [*Fu et al.*, 2009] and other species. Pixel size could also be increased, but this is not recommended since it would result in a greater fraction of observations lost due to clouds [*Bréon et al.*, 2005] and would also limit the ability to spatially resolve point source emissions [*Bovensmann et al.*, 2010].

Various types of HEOs can provide continuous or quasi-geostationary coverage, but all require at least two satellites to accomplish this. A Molniya 12 h HEO has been used on past Russian missions and is one option for PCW [*Trishchenko and Garand*, 2011]. *Trishchenko et al.* [2011] later compared the Molniya orbit with a Tundra orbit (24 h period) and a Three Apogee (TAP) orbit (16 h period), which indicated that the TAP orbit was best when all factors are considered, such as the altitudes of apogee (~43,500 km) and perigee (~8100 km), observational coverage, downlink opportunities, and reduced exposure to protons from the Earth's van Allen belts, thus making it the leading candidate orbit for the PCW mission.

3. Method

The primary experiment carried out in this work consists of three main steps:

1. Use a CO_2 model with realistic CO_2 fluxes to simulate a CO_2 distribution to be designated as the "Truth".

2. Create "synthetic observations" for LEO and HEO missions by sampling the simulated "true" fields at the hypothetical observation locations and times (accounting for orbit, sunlight, surface properties, clouds, etc.) then adding noise.

3. Beginning with an a priori state that differs from the "Truth", assimilate each set of synthetic observations to try to recover the "true" fluxes used to generate the synthetic observations, accounting for observation and model errors, and assess the error reduction in the flux estimates.

We will refer to this approach as an Observing System Simulation Experiment (OSSE), although the design is simpler than for most OSSEs in meteorological data assimilation, which usually focus on the added value of a new instrument to the global observing system, already consisting of a constellation of LEO and GEO operational missions. Near-term spaceborne CO_2 capabilities are much more limited, with only a small number of research satellites, thus the configuration of any future observing system is extremely uncertain, so we instead focus on the contribution from individual missions rather than how they would improve an assumed constellation.

3.1. Model Simulation

The model used to simulate CO_2 is GEOS-Chem (http://acmg.seas.harvard.edu/geos/) v8-03-02 with GEOS-5 meteorological fields at $2° \times 2.5°$ resolution and 47 vertical levels for 2009. GEOS-Chem includes a complete set of CO_2 fluxes (national fossil fuels, ocean, terrestrial biosphere, biomass burning, biofuel burning, international shipping and aviation, and a 3-D CO_2 chemical source from oxidation of other hydrocarbons) to represent the global carbon cycle [*Nassar et al.*, 2010]. These fluxes for 2009 were used, except the CO_2 chemical source was turned off for this work, Global Fire Emissions Database (GFED) v3 [*van der Werf et al.*, 2010] was used rather than GFED v2 and the standard terrestrial biosphere and ocean fluxes of the model were replaced by NOAA CarbonTracker [*Peters et al.*, 2007] v2010 optimized fluxes for 2009.

3.2. Generating Synthetic Observations
3.2.1. Observation Locations

The Space Environment Information System (http://www.spenvis.oma.be/intro.php) v.4.6.5 online orbit modeling tools were used with the GOSAT orbit parameters (Sun-synchronous orbit with an altitude of 665.96 km, inclination of 98.06°, and an equator crossing time of 12:49 for the ascending node) to generate coordinates for an orbit track as a function of time. GOSAT observation positions were determined for three cross-track observations, located along the orbit track and 263 km east and west, which is a reasonable approximation of the GOSAT observing pattern used since August 2010 according to the GOSAT Data Users Handbook [*Japan Aerospace Exploration Agency, National Institute for Environmental Studies, Ministry of the Environment*, 2011]. For simplicity, we assumed each complete cross-track scan sequence to take 1 min (which includes 4 s per scan and three scans for each cross-track point (from slightly different observing angles), plus along-track and cross-track turnaround times between observations).

The TAP orbit and the PCW meteorological imager viewing strategy are described in *Trishchenko et al.* [2011], although some details of the orbit and viewing are still to be determined. The viewing strategy for the PHEOS-FTS will differ from the meteorological instruments and is much less certain, so certain aspects of the viewing were assumed. Observation locations were determined for a TAP orbit with an apogee latitude of 64.0°N, which is close to the critical value of 63.435°N [*Trishchenko et al.*, 2011]. Apogee longitudes are separated by 120° at 95° W, 35°E, and 155°E. The FTS would have a Field of Regard (FOR) centered below each apogee that it would scan over a period of 80 min, up to 6 times per orbit. We propose a FOR covering an area of 4480×3360 km^2 (wider than some other proposed observing scenarios) consisting of 8×6 fields of view (FOVs), as shown in Figure 1. Each FOV would consist of a 56×56 pixel array of 10×10 km^2 pixels. Under this scenario, one FOR covers most of Canada including the entire Canadian permafrost region and most of the Boreal forest. Other areas of interest included are the Alberta oil sands, as well as the metropolitan areas of Vancouver, Edmonton, Calgary, Winnipeg, Quebec, and Seattle. Three of Canada's most populated metropolitan areas: Toronto, Montreal, and Ottawa-Hull are not included since they are south of the observation range, but these cities could be observed with a US-focused GEO mission. Newfoundland and some other parts of Atlantic Canada are also outside of the FOR as proposed, but potentially observable with some adjustments from HEO or also from GEO. The other two FORs would be centered on Europe and East Asia as shown in Figure 1.

It is proposed that the FTS stare at each FOV for approximately 100 s. The directional scan pattern of each FOV within the FOR has not been decided, so we assume scanning from east to west, then advancing north and beginning the next row of FOVs and repeating the earlier scan pattern from east to west again. Scanning an entire FOR in this way would require 80 min. We set the timing of each apogee to correspond with local noon, in order to maximize opportunities to observe during daylight and low solar zenith angle (see section 3.2.2). The instruments would not measure outside of the three FORs, thus each satellite could potentially obtain 8 h of viewing in a 16 h period, which combined gives 24 h of observations per day. We make the conservative assumption that the satellites would follow this observing pattern only 50% of the time, with other observing modes (such as all three FORs coincident over the north pole) at other times. The north polar observations would not yield viable NIR CO_2 observations, but would satisfy certain meteorological and air quality observing priorities. Due to the large data volume resulting from the FTS interferograms, a "checkerboard" pattern has been proposed where every other pixel in the 56×56 array is discarded to reduce the downlink volume by a factor of 2. The latitude (ϕ) and longitude (λ) of each observation point were determined by translating the (x,y)
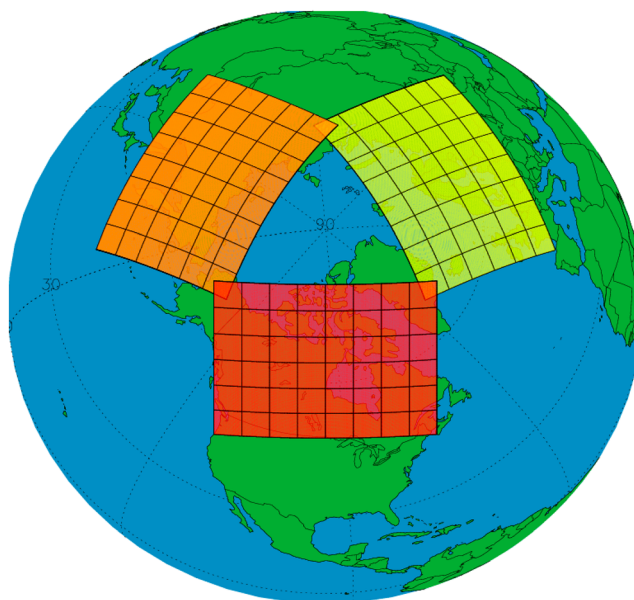
Figure 1. PCW-PHEOS-FTS observational coverage from two satellites in a 16 h TAP orbit showing the Fields of Regard (FORs) corresponding to the three apogees, which are centered on (95°W, 64°N), (25°E, 64°N), and (145°E, 64°N). Each square within a FOR is observed with a field of view (FOV) consisting of a 56×56 array of $10 \times 10 \ km^2$ pixels.

coordinates relative to the center of the FOR of each apogee with an orthographic projection [*Snyder*, 1993], as outlined in Appendix A.

3.2.2. Daylight, Albedo, and Cloud Filtering

Since NIR observations measure reflected sunlight, we determine sunlit times and solar zenith angles (SZA or θ) for all observation locations as described in Appendix B. Only observations with SZA $< 85°$ were retained. It is also necessary to account for surface properties that adequately reflect the solar radiation at the wavelengths of the O_2 *A* band (0.76 μm, 13,150 cm^{-1}) and weak CO_2 band (1.61 μm, 6210 cm^{-1}) from both GOSAT and PHEOS, and strong CO_2 band (2.06 μm, 4850 cm^{-1}) from GOSAT. The advanced very high resolution radiometer (AVHRR) $1° \times 1°$ land cover classification [*Hansen et al.*, 1998, 2000] assigns one of 13 different values corresponding to a surface type (or lack of data) for all global pixels. We simplify this scheme by aggregating values into six categories: 0 (water or sea ice); 1–3,5,11 (forests); 4 (tundra); 6,7 (grassland); 8,9 (predominantly bare ground / desert); 12 (data unavailable (typically ice caps, but any unavailable middle/low-latitude pixels were assigned a neighboring value), yielding the surface cover in Figure 2. By combining the AVHRR surface types with moderate resolution atmospheric transmission (MODTRAN) spectral albedos for different surfaces
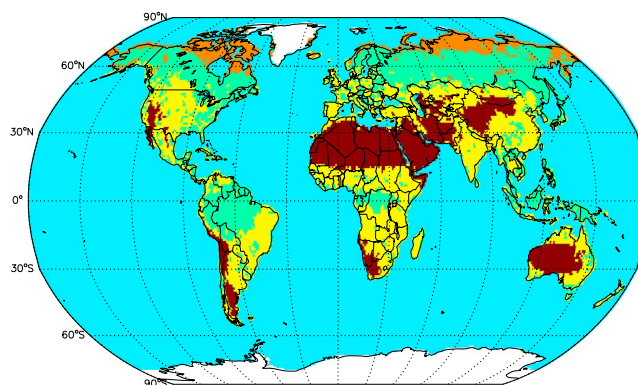

Figure 2. Simplified AVHRR $1° \times 1°$ surface types desert (brown), grassland/savanna (yellow), forest (green), tundra (orange), water (blue), and year-round snow (white).
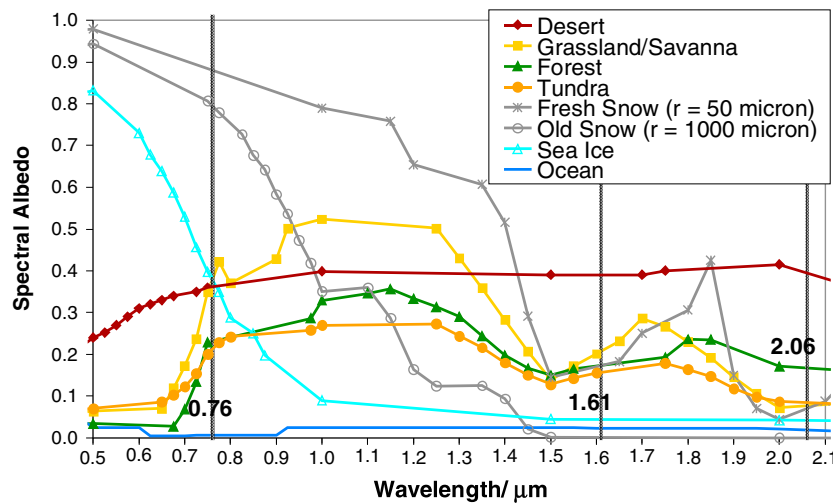
Figure 3. Spectral albedo for different surface types based on the MODTRAN database.

shown in Figure 3 [*Berk et al.*, 2008], one obtains maps of albedo at 1° × 1° for each spectral band. Nadir observations over the ocean, sea ice, and snow/ice caps (Antarctica, Greenland, Svalbard, and Ellesmere and Sverdrup Islands) are ruled out due to low albedo. GOSAT has ocean glint capability within ±20° from the subsolar latitude, which varies throughout the year. We assumed fixed monthly subsolar latitudes (−15°, −7.5°, 0°, 7.5°, 15°, 22.5°, 15°, 7.5°, 0°, −7.5°, −15°, and −22.5°) and GOSAT glint observations within ±20° of this latitude. No glint capability was assumed for the PHEOS-WCA mission.

In simulated OCO-2 retrievals by *Boesch et al.* [2011], larger errors are found over snow or ice due to its low albedo in the CO_2 bands, but these observations were not ruled out. Unfortunately, snow parameters such as wetness, grain size, or impurities complicate predictions of the feasibility of observations over snow-covered surfaces. (Black carbon in snow is an impurity with major impacts on albedo [*Schwarz et al.*, 2013], which could increase in importance as anthropogenic activity in the Arctic increases.) MODTRAN gives very different values for the albedo of fresh snow (grain radius = 50 μm) and old snow (*r* = 1000 μm) as shown in Figure 3. Using GEOS-5 snow depth values at the native resolution (0.5° × 0.667°, 3 h), seasonal snow coverage was determined for all observation locations and times. For both GOSAT and PHEOS-WCA, we generate two separate sets of observation locations and times. In one set, observations over seasonal snow greater than 1 cm in depth are excluded, while in a second set they are included, but will be used with lower precision than over other land surfaces (described in section 3.2.3). Due to the different resolutions between AVHRR surfaces types (1° × 1°) and GEOS-5 snow depth (0.5° × 0.667°), coastal marine observations or those over large lakes can mistakenly be retained as land observations and found to be snow free, so we also remove GOSAT or PHEOS-WCA nadir observations where the GEOS-5 land fraction is less than 0.5 to overcome this problem.

Only observations that are not obstructed by clouds will lead to successful retrievals. To remove cloudy observations, only those in a grid box with a cloud fraction (GEOS-5, 0.5° × 0.667°, 3 h) less than 0.05 are retained. This simple approach would be a poor approximation with coarse resolution meteorological fields due to subgrid heterogeneity, but is reasonable at 0.5° × 0.667° resolution since 0.5° latitude is ~55.6 km and 0.667° longitude is only ~74.1 km at the equator, ~52.4 km at 45°N, and matches the footprint dimension (10 km) at 82.2°N.

These GOSAT and PHEOS-WCA cloud, albedo (with and without snow) and SZA filtered observation locations and times were then used to sample the simulated 3-D CO_2 distributions to produce a pair of 1 year CO_2 observation data sets for each mission. Lastly, random noise was added to each data set (with a different seed for each month, instrument configuration, and snow scenario), with an amplitude proportional to the observation error covariance.

3.2.3. Averaging Kernel and Error Covariance
GOSAT Level 2 data from the National Institute for Environmental Studies (NIES) include both column averaging kernels and full averaging kernel matrices [*Yoshida et al.*, 2011], which define the vertical sensitivity of the observed

profile on the retrieval grid. Using the land surface classification from the previous section, we separated July 2009 v2.0 retrievals by the surface types: forest, tundra, grasslands, desert, and ocean (glint) to calculate a mean averaging kernel matrix for each surface type to be used as the vertical sensitivity in both LEO and HEO observations.

The same approach was used with the GOSAT NIES error covariance matrices for the GOSAT observations. PHEOS error covariances are calculated by scaling the GOSAT covariance matrices according to the change in SNR between the instruments for a common albedo and SZA. The GOSAT SNR is >300 for the O_2 A band and CO_2 bands (surface albedo of 0.3, SZA of 30°, 6.8 cm aperture, 4 s scan [*Yokota et al.*, 2009]). PHEOS observations are made from a much greater distance, reducing the signal, but the FTS will scan for 100 s to reduce noise. Phase 0/A studies demonstrated SNRs of >100 (CO_2) and >110 (O_2 A) for the Lite configuration (10 cm aperture) and >150 (CO_2) and >160 (O_2 A) for the Optimal configuration (15 cm aperture) for a surface albedo of 0.4 and SZA of 60° (PHEOS-WCA Phase A Closure Report; Tables 11–12, Northeast Space Company Report for Environment Canada). To estimate GOSAT SNR at a SZA of 60° rather than 30°, we multiply by $\sqrt{\cos(60°)/\cos(30°)} = 0.7598$, giving SNR >228. To estimate the PHEOS-FTS SNR at an albedo of 0.30 rather than 0.40, we multiply the mean SNR of the CO_2 and O_2 A bands by $\sqrt{0.30/0.40} = 0.8660$, giving SNR > 91 for the Lite configuration and SNR > 134 for the Optimal configuration. Therefore, to obtain PHEOS error covariances, GOSAT covariances are multiplied by the square of the GOSAT/PHEOS ratio of SNRs $(228/91)^2 = 2.5^2$ (Lite) or $(228/134)^2 = 1.7^2$ (Optimal), effectively assigning a lower precision (and more noise) to each PHEOS observation by a factor of 2.5 or 1.7.

At present, most observations over snow-covered surfaces are filtered out for both the NIES and Atmospheric Carbon Observations from Space GOSAT Level 2 XCO_2 retrievals [*O'Dell et al.*, 2012; *Crisp et al.*, 2012] due to biases that are poorly understood. Although XCO_2 retrievals over snow are challenging, they are technically possible over fresh snow based on experimentally derived spectral albedos, thus, we consider the retrieval of XCO_2 from observations over snow to be an area requiring further investigation. In section 3.2.2, we generated two data sets for each mission, one with observations over snow and one without. When using the snowy data set, for both the GOSAT and PHEOS observations located where snow depth is greater than 1 cm, covariances were multiplied by 4, reducing the precision of these observations by a factor of 2, which is similar to the reduction in precision found in simulated OCO-2 retrievals [*Boesch et al.*, 2011]. For shallower snow ($<$ 1 cm), the underlying vegetation is assumed to remain the dominant factor determining albedo.

3.3. Surface Flux Inversion

Our approach for the source/sink inversion in this work is an analytical Bayesian inversion. The state vector consists of monthly fluxes from predefined spatial regions: 32 land regions, 11 ocean regions, and 1 ice region. The land regions are shown in Figure 4, while the ocean regions are the same as in the Atmospheric Tracer Transport Model Intercomparison Project (TransCom) experiments [*Gurney et al.*, 2002] and we optimize the land biosphere and ocean fluxes (with fixed fossil fuel emissions) as in TransCom. Optimization of monthly surface fluxes is carried out using a maximum a posteriori approach by minimizing the cost function:

$$J(\mathbf{x}) = (\mathbf{y} - \mathbf{F}(\mathbf{x}))^{\mathsf{T}}\mathbf{S}_y^{-1}(\mathbf{y} - \mathbf{F}(\mathbf{x})) + (\mathbf{x} - \mathbf{x}_a)^{\mathsf{T}}\mathbf{S}_x^{-1}(\mathbf{x} - \mathbf{x}_a) \tag{1}$$

where $\mathbf{y}$ is the observation vector that consists of the retrieved satellite CO_2 profiles, $\mathbf{x}$ is the state vector with elements representing the CO_2 flux from each region, $\mathbf{x}_a$ is the a priori state vector, $\mathbf{S_y}$ is the observation error covariance matrix, and $\mathbf{S_x}$ is the a priori covariance matrix for the fluxes. The forward model $\mathbf{F}(\mathbf{x})$ reflects the transport of the CO_2 perturbations that result from the fluxes, and is given by

$$\mathbf{F}(\mathbf{x}) = \mathbf{y_a} + \mathbf{A}\left[\mathbf{H}(\mathbf{x}) - \mathbf{y_a}\right] \tag{2}$$

where $\mathbf{H}(\mathbf{x})$ is the model CO_2 profile interpolated to the retrieval grid, $\mathbf{y}_a$ is the a priori CO_2 profile for the satellite retrieval, and $\mathbf{A}$ is the averaging kernel matrix.

The optimal a posteriori estimates of the state vector $\hat{\mathbf{x}}$ and the covariance matrix $\hat{\mathbf{S}}$ that minimize the cost function are given by

$$\hat{\mathbf{x}} = \mathbf{x_a} + \mathbf{S_x}\mathbf{K}^{\mathsf{T}}\left(\mathbf{K}\mathbf{S_x}\mathbf{K}^{\mathsf{T}} + \mathbf{S_y}\right)^{-1}(\mathbf{y} - \mathbf{K}\mathbf{x_a}) \tag{3}$$

$$\hat{\mathbf{S}} = \mathbf{S}_x + \mathbf{S_x}\mathbf{K}^{\mathsf{T}}\left(\mathbf{K}\mathbf{S_x}\mathbf{K}^{\mathsf{T}} + \mathbf{S_y}\right)^{-1}\mathbf{K}\mathbf{S}_x \tag{4}$$

where $\mathbf{K}$ is the Jacobian, which gives the sensitivity of the CO_2 abundances to the surface fluxes ($\mathbf{K} = \partial\mathbf{F}(\mathbf{x})/\partial\mathbf{x}$). The Jacobians used above were determined in the following way. A model simulation was carried out in
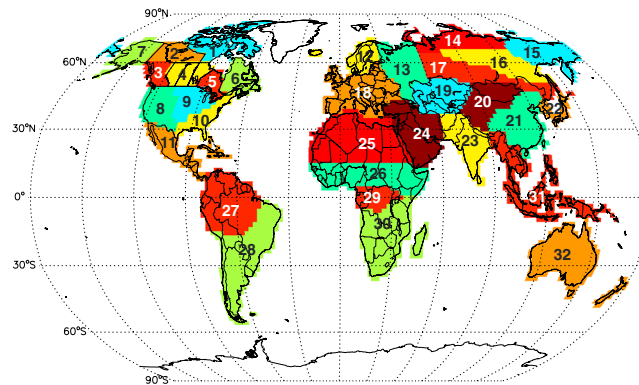
Figure 4. Thirty-two land regions used for the inversion along with the 11 TransCom ocean regions and an ice region (mainly composed of Greenland and Antarctica, with virtually no flux), for a total of 44 regions.

which the CO_2 from each surface flux was tagged as a separate tracer. The simulation was run for 2 years including a 1 year spin-up (which is discarded) and the simulation year. A background tracer (exposed to the model transport and background fluxes, but not the biospheric/oceanic fluxes), was then subtracted from each of the tagged tracers and the differences were normalized by dividing each by their respective surface flux. Limitations of this approach are discussed in section 5.

Observation-model differences are determined by sampling the model at the $2° \times 2.5°$ grid box within ± 1 h of the observation then calculating monthly averages at the grid scale. By annually aggregating CarbonTracker fluxes for 2007–2009 to our regions, then finding the standard deviation of the monthly flux σ_{CT}^i for each region i, the fluxes and their interannual variability can be used to construct our a priori flux vector $\mathbf{x}_a$ and a priori covariance matrix $\mathbf{S}_x$. The interannual variability of biospheric (or oceanic) fluxes is expected to be a major component contributing to flux uncertainty, although it does not account for any inadequacy in observational coverage to constrain these fluxes; thus, the standard deviation of the flux for each region can be thought of as a lower limit on the a priori flux uncertainty for that region. The diagonal of the a priori covariance matrix was thus set to be proportional to the standard deviation of the flux for a given month over the 3 year period according to

$$S_x^{ii} = \left(\gamma \sigma_{CT}^i \right)^2 \tag{5}$$

where γ is a scale factor that we set to 2 to account for additional uncertainty not represented by the standard deviation of CarbonTracker interannual variability. A priori and a posteriori uncertainty vectors ($\boldsymbol{\sigma}_a$ and $\boldsymbol{\sigma}$) for each month are equal to the square root of the diagonal of their respective covariance matrix $\mathbf{S}_x$ or $\hat{\mathbf{S}}$.
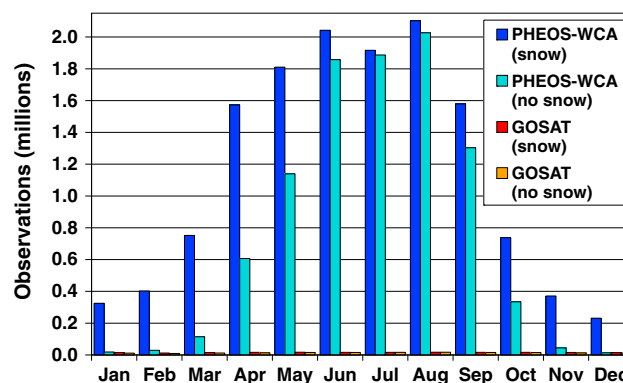

Figure 5. Number of simulated observations globally per month from GOSAT and PCW-PHEOS-WCA after filtering for surface albedo, clouds, and solar zenith angle. Two scenarios are shown for each mission—one where observations over snow are included (labeled as "snow") and another where they are excluded (labeled as "no snow").

The annual fluxes (true, prior, or posterior) are determined simply as the sum of the 12 monthly fluxes and the annual flux uncertainties (prior or posterior) are determined as

$$\sigma_{\text{annual}} = \left[\sum_{n=1}^{12} \sigma_n^2 \right]^{1/2} \tag{6}$$

Using the above described inverse modeling approach, we compare the posterior fluxes $\hat{\mathbf{x}}$ and uncertainties from GOSAT observations and from PHEOS-WCA observations using a TAP orbit and two different instrument configurations: Optimal and Lite, under scenarios where observations over snow are included or excluded.

4. Results

4.1. Number of Simulated Observations

The numbers of simulated observations from GOSAT and PHEOS for each month are compared in Figure 5 showing one scenario where observations over snow are included in the count and another where they are excluded. The mean values of 14,973 GOSAT observations per month including those over snow, or 13,031 observations per month excluding those over snow, bracket the actual mean of 14,393 observations per month for the first full year of GOSAT NIES v2.0 Level 2 data (June 2009 to May 2010), in which most observations over snow will have been screened out. The consistency between the simulated and real GOSAT observation numbers demonstrates that our simulated GOSAT observational coverage is realistic. The number of PHEOS observations peaks in Northern Hemisphere (NH) summer at 1.8–1.9 million/month and is orders of magnitude lower in the winter, primarily due to the shortened duration of daylight and larger SZAs.

The simulated GOSAT observation distribution indicates much less change with season since the Sun-synchronous observations are only made near midday. In general, since each PHEOS observation has a lower SNR, it will be less precise, but the very large number of observations enables averaging to improve the SNR/precision of the mean. The actual number of PHEOS observations will depend on the final mission design constraints and the viewing schedule. Here we have assumed a very conservative observing scenario, with a checkerboard pattern to thin the data and XCO_2 observations only made half of the time to accommodate other observational modes at other times. One such mode would have the FORs centered on the north pole for weather and air quality purposes using the TIR and UVS bands, but insufficient NIR albedo for XCO_2 retrieval. The checkerboard pattern and restricted viewing time imposed each reduce the number of observations by a factor of 2 from what is potentially possible. The number of observations per month per $1° \times 1°$ grid box for each mission, after the filtering is shown in Figures 6 (including observations over seasonal snow) and 7 (excluding observations over seasonal snow). During the winter months (December, January, and February) PHEOS obtains only a few thousand snow-free observations, which are barely visible in Figure 7, mainly located over the North American west coast (southern British Columbia, Washington, and Oregon), the British Isles, France, Germany, Poland, and occasionally over Atlantic Canada. For inversion scenarios where observations over seasonal snow-covered surfaces are included, the observations over snow are used with a degraded precision relative to surfaces with higher NIR albedos (as described in section 3.2.3).

4.2. Fluxes and Uncertainties

Monthly CO_2 fluxes and uncertainties were determined from simulated observations from GOSAT and the two PHEOS instrument configurations (Optimal and Lite), with and without observations over snow. The posterior flux uncertainties from the posterior covariance matrices ($\sigma^i = \sqrt{S^{ii}}$) from GOSAT exhibit more uniform reductions across regions relative to the prior uncertainties ($\sigma_a^i = \sqrt{S_x^{ii}}$), while PHEOS observations constrain the northern regions, which it observes, much better than regions not observed, as expected. This results in superior uncertainty reduction from PHEOS for the Arctic and boreal latitudes, while for lower NH latitudes and the Southern Hemisphere, the uncertainty reductions are better from GOSAT.

Monthly fluxes and uncertainties for the 14 northern regions observed by the PHEOS-FTS are shown in Figure 8. All regions show a similar seasonal pattern with peak biospheric uptake (negative flux) during the summer. For Ontario, Eastern Canada, and Northern Siberia, both the phase and amplitude of the seasonal cycle of CO_2 flux show little difference between the a priori and the truth (since CarbonTracker had little interannual variability for these fluxes over the 3 year period) so the inversions easily constrain these fluxes with all the observational data sets that we compare. For Nunavut and Islands, Yukon and Northwest Territories, British Columbia and Eastern
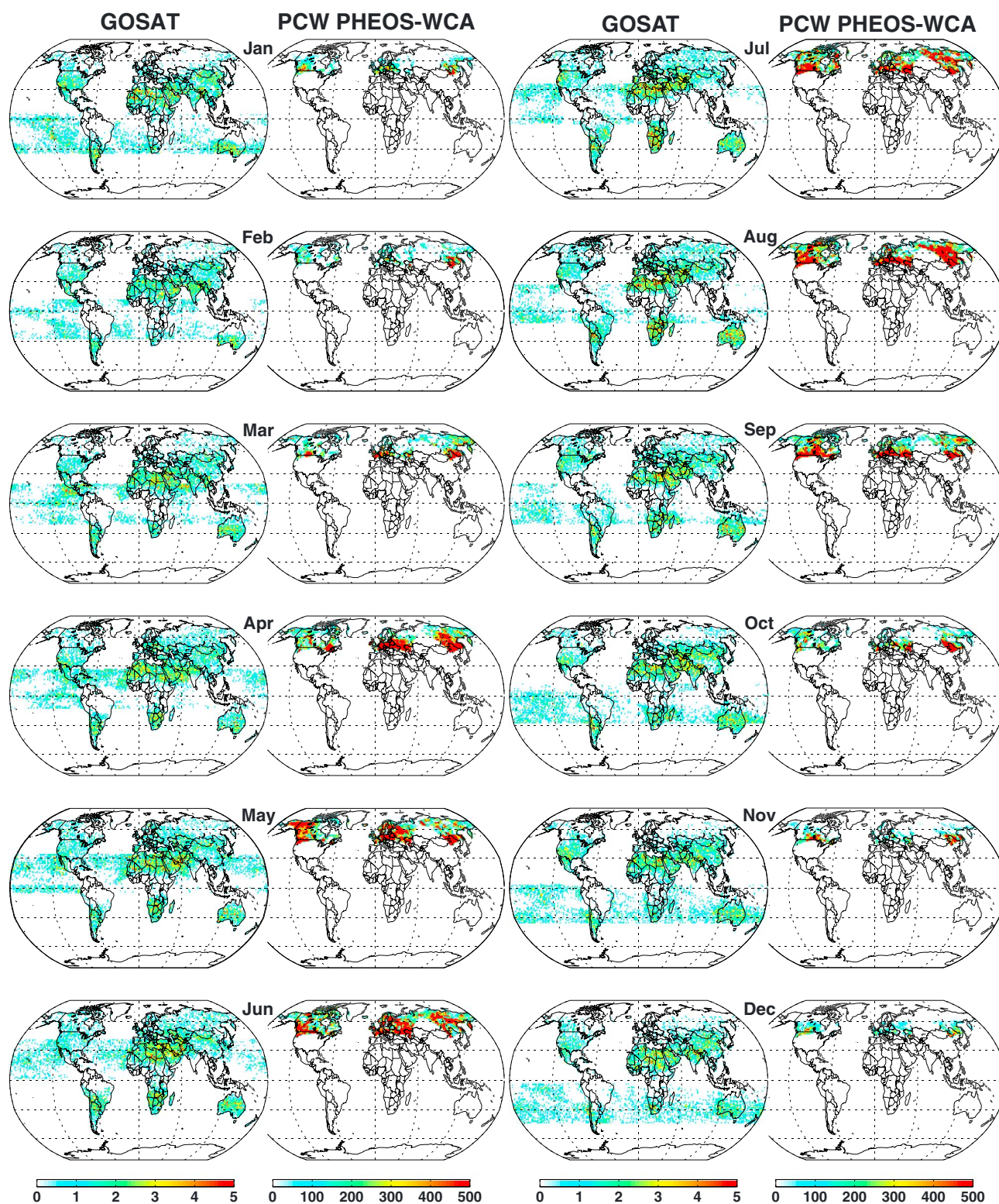
Figure 6. Number of simulated observations per month per 1° × 1° grid cell from GOSAT and from the PCW-PHEOS-WCA mission, after filtering for SZA, albedo, and clouds. Observations over seasonal snow are included. (Note the different color scales for each mission.)
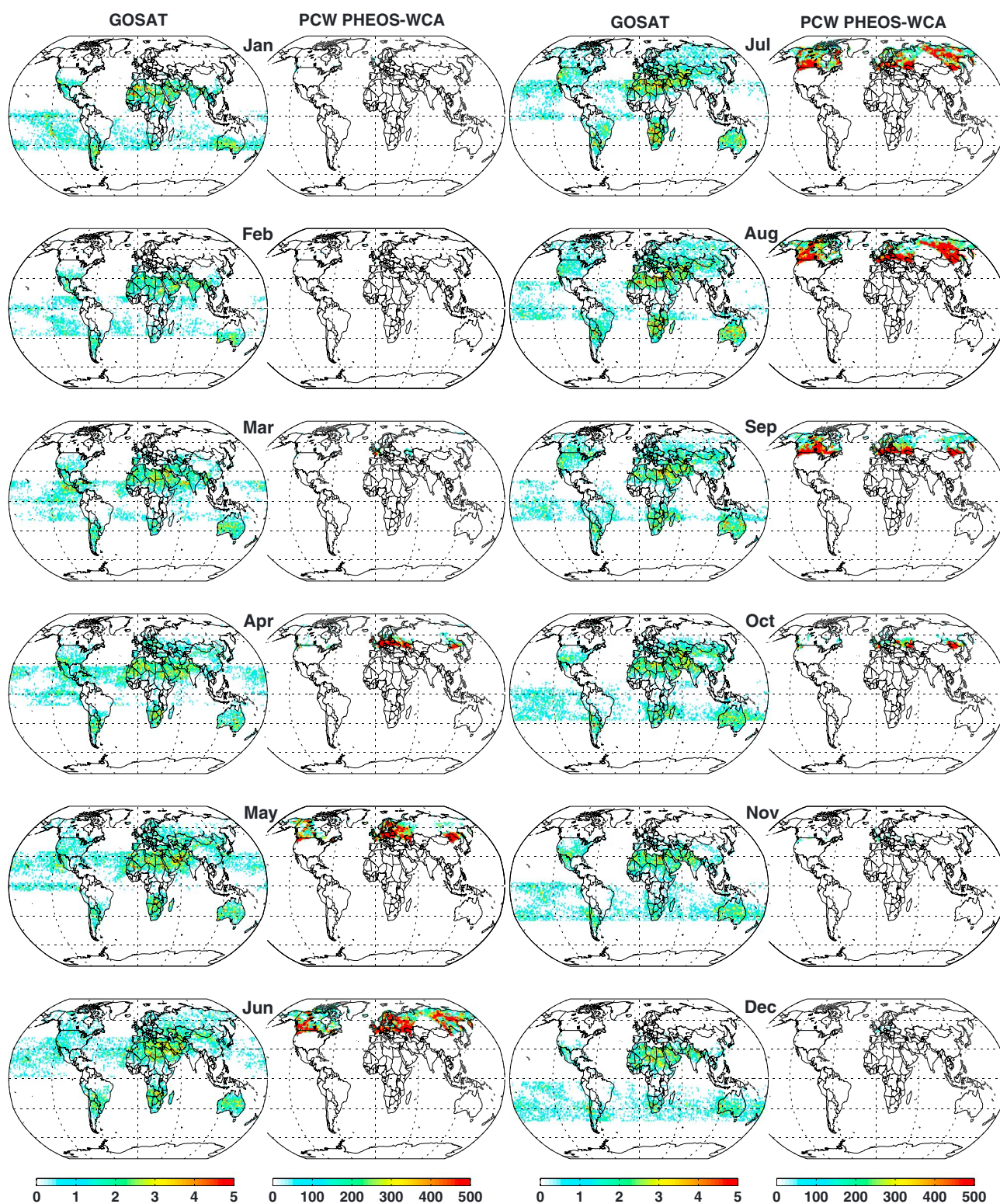
Figure 7. Same as Figure 6 but excluding observations over seasonal snow. (Note the different color scales for each mission.)

Siberia, the prior had the correct seasonality with an incorrect amplitude, while for the Canadian Prairies, Alaska, Scandinavia, South and Central Europe, Eastern Europe, Central Siberia, and Southern Siberia the prior seasonality differed from the truth. In cases where the amplitude or seasonality differed between the prior and the truth, PHEOS posterior fluxes match the true profile slightly better than the GOSAT posterior fluxes do,
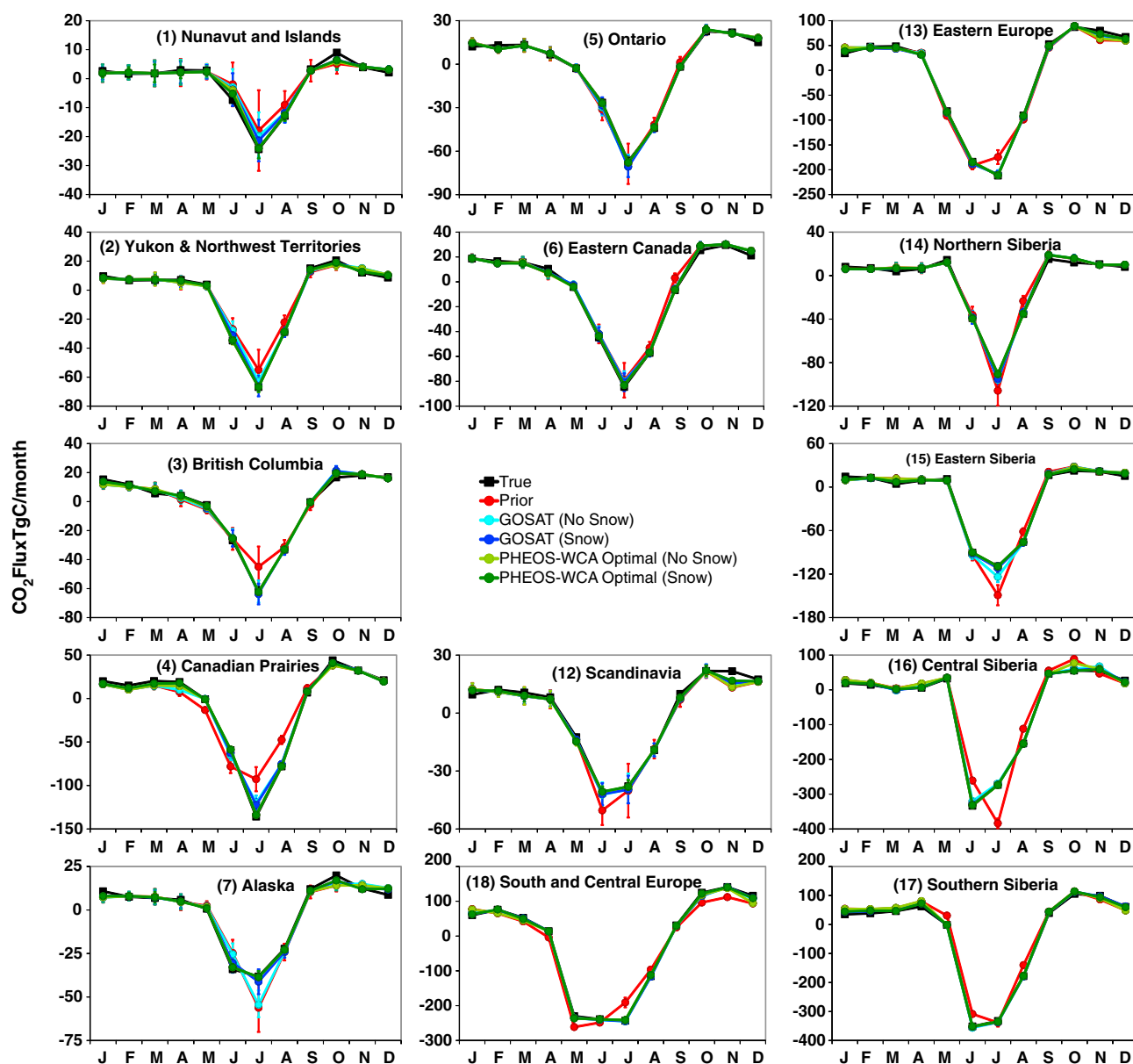
Figure 8. Monthly fluxes and uncertainties (TgC/month) for the 14 northern regions observed from the TAP orbit. True fluxes, prior fluxes, fluxes derived from GOSAT observations including/excluding observations over snow, and fluxes derived from PHEOS-WCA observations including/excluding observations over snow are compared. The largest differences and uncertainties are seen during summer months, when PHEOS-WCA observational coverage peaks.

particularly for the summer minimum. Nunavut and Islands, Canadian Prairies and Alaska are good examples of regions where this occurs. The prior and the truth occasionally differ in the autumn (i.e., Nunavut and Islands and South and Central Europe), which is a time period more difficult for either of the missions to constrain due to the reduced number of high-latitude observations, especially when all observations over snow are excluded.

The benefit of the PHEOS-WCA mission for constraining annual biospheric fluxes for Arctic and boreal latitudes is shown in Table 2 and illustrated by Figure 9, showing the ratio of posterior uncertainty (σ) from each PHEOS configuration relative to the posterior GOSAT uncertainty for the same regions shown in Figure 7. The uncertainty ratio is arguably a more robust measure than the absolute uncertainty in Table 2, since it is not sensitive to assumptions about prior uncertainties. Not surprisingly, the Optimal instrument configuration clearly yields lower uncertainties for all observed regions than the Lite configuration. Ratios less than unity imply that the PHEOS observations can more precisely constrain the fluxes than the GOSAT observations, which is found for 12 of 14 regions, with South and Central Europe and Southern Siberia as the exemptions. South and Central Europe

Table 2. True Flux, Prior Flux and Uncertainty, and the Posterior Flux and Uncertainty for GOSAT and Two PHEOS-WCA Instrument Configurations, With Snow Observations Included/Excluded (TgC/yr)[a]

	True $\mathbf{x}_{TRUE}$	Prior $\mathbf{x}_a \pm \sigma_a$	GOSAT		PHEOS-WCA Optimal		PHEOS-WCA Lite	
			Snow $\hat{\mathbf{x}} \pm \sigma$	No Snow $\hat{\mathbf{x}} \pm \sigma$	Snow $\hat{\mathbf{x}} \pm \sigma$	No Snow $\hat{\mathbf{x}} \pm \sigma$	Snow $\hat{\mathbf{x}} \pm \sigma$	No Snow $\hat{\mathbf{x}} \pm \sigma$
(1) Nunavut and Islands	−14.5	−3.4 ± 8.9	−10.2 ± 7.7	−8.0 ± 8.2	−15.1 ± 5.6	−14.4 ± 6.2	−13.9 ± 6.4	−13.5 ± 6.8
(2) Yukon and NW Territories	−40.0	−17.6 ± 17.0	−38.5 ± 12.4	−32.1 ± 14.7	−41.7 ± 6.9	−42.8 ± 8.6	−41.8 ± 8.7	−42.2 ± 9.8
(3) British Columbia	−36.6	−21.8 ± 19.1	−35.3 ± 12.3	−37.9 ± 13.9	−33.9 ± 7.3	−36.7 ± 9.5	−33.8 ± 9.2	−36.6 ± 10.8
(4) Canadian Prairies	−95.9	−80.4 ± 37.4	−102.9 ± 17.9	−108.9 ± 21.8	−107.8 ± 10.0	−117.2 ±13.9	−108.8 ± 12.7	−116.2 ± 15.3
(5) Ontario	−37.6	−34.6 ± 17.9	−38.8 ± 11.3	−39.6 ± 12.8	−34.8 ± 8.0	−34.2 ±8.2	−35.2 ± 9.2	−35.0 ± 9.3
(6) Eastern Canada	−60.0	−34.1 ± 16.8	−47.5 ± 12.9	−46.0 ± 13.6	−54.2 ± 10.3	−53.6 ± 11.6	−51.4 ± 11.6	−50.9 ± 12.5
(7) Alaska	−9.9	−23.5 ± 23.6	−14.2 ± 13.0	−21.9 ± 20.3	−13.0 ± 8.1	−14.0 ± 10.5	−13.7 ± 9.9	−14.0 ± 11.4
(12) Scandinavia	0.1	−25.8 ± 26.8	−14.2 ± 11.8	−15.2 ± 12.9	−10.0 ± 7.8	−14.2 ± 10.2	−11.8 ± 9.2	−14.7 ± 10.9
(13) Eastern Europe	−118.0	−130.7 ± 66.6	−142.4 ± 29.8	−141.3 ± 37.1	−135.6 ± 19.8	−141.3 ±33.1	−139.8 ± 24.8	−143.1 ± 35.3
(14) Northern Siberia	−79.8	−72.4 ± 24.8	−74.9 ± 15.6	−75.3 ± 18.5	−72.6 ± 11.0	−72.4 ± 11.7	−72.8 ± 13.1	−72.8 ± 13.6
(15) Eastern Siberia	−148.2	−160.7 ± 54.2	−144.6 ± 18.9	−154.7 ± 33.6	−144.6 ± 10.4	−135.7 ± 14.9	−143.3 ± 12.9	−135.2 ± 16.1
(16) Central Siberia	−503.7	−440.6 ± 164.8	−489.7 ± 27.4	−457.1 ± 44.0	−495.4 ± 18.2	−452.9 ± 37.3	−489.2 ± 24.1	−451.0 ± 39.9
(17) Southern Siberia	−378.8	−220.6 ± 92.2	−343.6 ± 36.1	−335.9 ± 45.5	−343.3 ± 40.7	−325.6 ± 47.2	−333.1 ± 47.5	−322.7 ± 51.5
(18) Central and Southern Europe	−214.0	−290.0 ± 114.7	−238.7 ± 32.4	−242.5 ± 36.6	−225.6 ± 26.4	−246.7 ± 46.3	−232.8 ± 35.5	−259.2 ± 51.5

[a]CO_2 fluxes shown correspond to the sum of photosynthetic uptake, respiration emission, and biomass burning emission as well as any other terrestrial biospheric phenomenon such as microbial respiration emissions from soil and/or permafrost thaw.

(Region 18) is not a boreal or Arctic region and it is only partially sampled by PHEOS across the north, so the observations fail to capture the spatial and temporal nonuniformity in the true fluxes within the region. Southern Siberia (Region 17) is also only partially sampled from our TAP orbit, with much of the region falling between two FORs. Figure 8 demonstrates that observations over the region still yield a posterior seasonal flux pattern resembling the truth, but Figure 9 shows that PHEOS only offers similar constraints to GOSAT on an annual basis. A Molniya orbit, with four apogees, would provide better constraints than a TAP orbit in this specific case.

The mean annual uncertainties of the 13 Arctic and boreal regions (all earlier regions except South and Central Europe) relative to GOSAT are shown in Table 3. Annual uncertainties for the Optimal configuration are ~30% lower than from GOSAT, while for the Lite configuration they are ~20% lower than from GOSAT, with little difference between scenarios including or excluding observations over snow. (Uncertainty ratios would be slightly
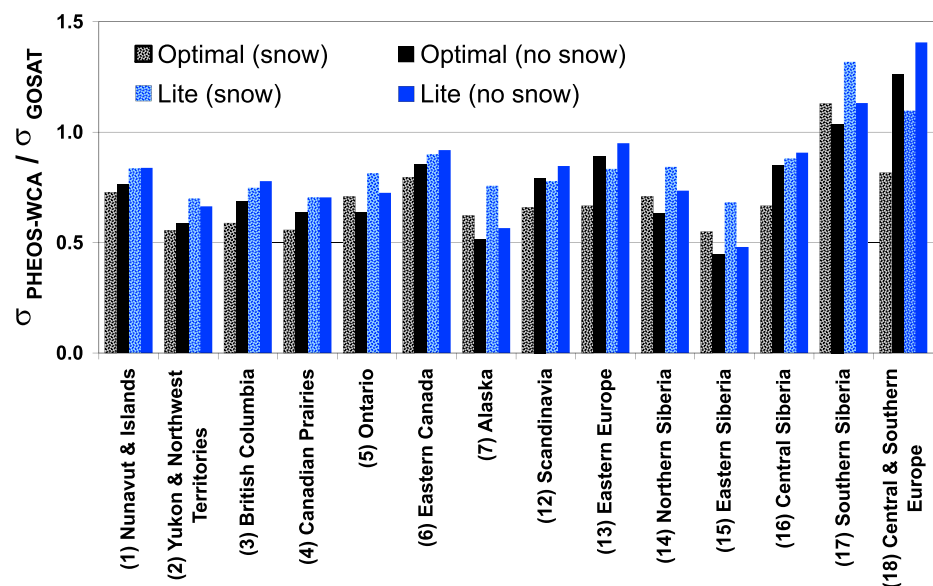

Figure 9. PHEOS-WCA a posteriori uncertainties ($\sigma_{PHEOS-WCA}$) for regions observed from a TAP orbit relative to the GOSAT a posteriori uncertainties (σ_{GOSAT}) for the two PHEOS-WCA instrument configurations. Lower ratios correspond to a larger error reduction.

Table 3. Annual CO_2 Flux Uncertainties Averaged for All Arctic and Boreal Regions (Regions 1–7, 12–17) From Observations by PHEOS-WCA Relative to Observations by GOSAT ($\sigma_{PHEOS}/\sigma_{GOSAT}$)

Configuration	Inclusion of Observations Over Seasonal Snow	June-July-August	Annual
Optimal	Yes	0.54	0.69
Optimal	No	0.55	0.72
Lite	Yes	0.72	0.83
Lite	No	0.74	0.79

more favorable for PHEOS-WCA if Southern Siberia (Region 17) was excluded). All PHEOS uncertainty reductions improve if focused on the June-July-August period, when observational coverage is densest and prior flux uncertainties are also the largest. Fortunately (from an observational standpoint), these summer months are also the most likely time for periods of increased photosynthetic uptake, boreal forest burning, or permafrost thaw.

Additional inversion tests (not shown) in which the seasonal cycle is a hard a priori constraint (rather than our monthly approach that enables the posterior seasonal cycle to differ from the prior) resulted in larger annual reductions in uncertainty relative to GOSAT. This occurred because the dense CO_2 observations from PHEOS during spring, summer, and fall help to constrain the winter fluxes when a fixed seasonal cycle is assumed. Our choice of conducting the inversion at a subannual scale was mainly aimed at avoiding unrealistic annual constraints from summer observations. The specific choice of solving for monthly fluxes for which the observations constrain only their own month was primarily based on ease of implementation in our code, but it is close to the CarbonTracker assimilation window length of 5 weeks [*Peters et al.*, 2007]. Determining the optimal assimilation window period is not straightforward, and since it relates to observation density, it will likely differ for GOSAT, OCO-2, or a HEO (or GEO) mission, making it a topic that requires much further study (see discussion in section 5).

In our flux inversion approach, we have not explicitly accounted for observation correlations or observation error correlations, thus observation uncertainties reduce with averaging by a factor of $\sqrt{N}$ with no limit. This would only be realistic if the total observation uncertainty is fully dominated by noise with no bias present. A simple method to test the sensitivity of this assumption, without actually applying observation error correlations or assuming a bias, is to set a maximum value of N, after which point no reduction in uncertainty is obtained by averaging. This was tested with values of $N_{max} = 25$, 100, 400, and 900 (per month) to compare with the earlier assumption of $N_{max} = \infty$, as shown in Figure 10. Lower values of N_{max} imply that the observation uncertainty is dominated by biases rather than noise, while higher values imply the reverse. The strictest constraint, $N_{max} = 25$ translates to a maximum error reduction of a factor of 5 by averaging, suggesting that 20% of the original error cannot be removed by averaging and corresponds to a systematic error or bias. For an initial observation error of 5 ppm this
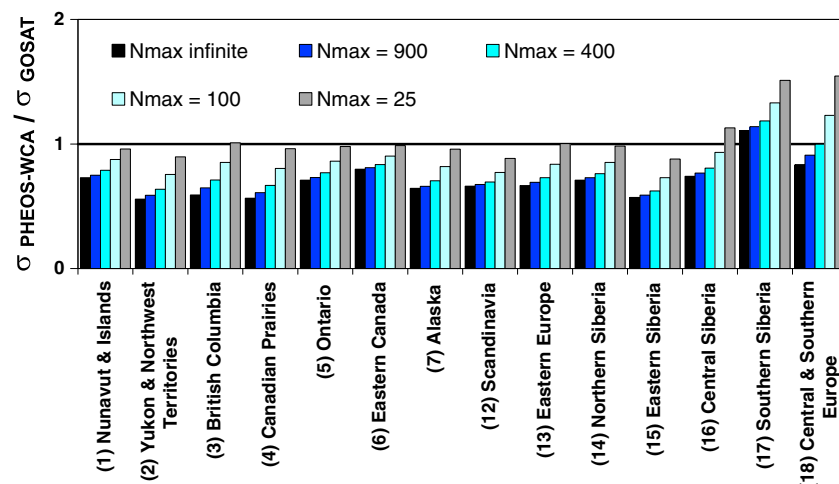

Figure 10. The change in the relative posterior error for the Optimal configuration (including observations over snow) assuming different values of N_{max}, which sets a threshold number of observations per month beyond which averaging does not reduce the total observation uncertainty. Lower ratios correspond to a larger error reduction. Lower values of N_{max} imply that the observation uncertainty is dominated by biases rather than noise, while higher values imply the reverse.

translates to 1 ppm bias, which on the order of current GOSAT XCO_2 retrieval biases [*Butz et al.*, 2011; *Crisp et al.*, 2012; *Yoshida et al.*, 2013; *Wunch et al.*, 2011]. XCO_2 retrieval biases will likely be lower in the PCW era (~2020s) as laboratory spectroscopic line parameters, retrieval methods, and validation methods improve. With $N_{max} = 25$, the posterior uncertainties for northern regions from PHEOS are only slightly better than LEO ($\sigma_{PHEOS}/\sigma_{GOSAT} \approx 1$), but for all other values of N_{max}, PHEOS posterior uncertainties are much lower for these regions.

5. Discussion

We have presented an OSSE to demonstrate the improved constraints on Arctic and boreal biospheric CO_2 fluxes from a HEO mission with the capabilities of the proposed PCW-PHEOS-WCA concept relative to a LEO mission with the capabilities of GOSAT. It should be noted that these are just representative HEO and LEO missions. Upcoming LEO missions like OCO-2, TanSat, or the proposed CarbonSat will differ with respect to orbit, pixel size and configuration, swath, spectral resolution, and SNR, and therefore could certainly yield different results. GOSAT was used for comparison since it is currently operating with proven capabilities and the TANSO-FTS design most closely resembles the proposed PHEOS-FTS.

Some assumptions were necessary to conduct the OSSE, since the true orbit or instrument characteristics were not available at the time of our experiments. Furthermore, we have adapted a FOR consisting of 6×8 FOVs (instead of 6×7, as recently suggested in the PHEOS-WCA concept proposal) in an attempt to span Canada, which would require some changes to instrument pointing. We also assumed the TAP orbit would be timed to maximize viewing opportunities during daylight hours, which is important for NIR and UVS, though less so for TIR emission or the meteorological imagers, but we also reduced the number of NIR observations to accommodate other viewing priorities and thin the data.

Retrieving XCO_2 over snow-covered surfaces is presently a challenge, so scenarios including and excluding these observations in our OSSE were carried out. Since observations over snow account for a nonnegligible fraction of Arctic and boreal observations, we chose not to completely reject these observations for two reasons. First, retrievals are continually improving such that some of the challenges associated with retrieving over snow may eventually be overcome, and second, because northern springtime snow cover has been declining at a rate (17.8%/decade for June 1979–2011) [*Derksen and Brown*, 2012] that is even faster than September sea ice loss over the past ~30 years. For these reasons, the associated challenges with observing over snow in the PCW mission timeframe (~2020s) could perhaps be reduced relative to the 2009 meteorological fields used in this work. We also used a rather strict definition of snow cover (a threshold of 1.0 cm) while in reality, the actual depth of snow required to impact the albedo will depend strongly on the vegetation cover, such that even smaller depths may be sufficient to change the albedo of barren land, but for a forest, whether the snow falls to the forest floor or stays on the canopy is more crucial than the actual snow depth. Other threshold values for snow depth were explored, but in practice, flux uncertainties or biases were very insensitive to this threshold.

Table 2 shows that absolute uncertainties would be much lower for either GOSAT or PHEOS-WCA if observations over snow gave adequate retrievals, suggesting that efforts to salvage these observations from current missions would be of value. However, Table 3 shows that the exercise of including and excluding the snowy observations in different inversion scenarios demonstrated that as long as the treatment of snow is the same for both missions, their ratio of uncertainties changes very little. This might suggest that potential problems with other assumptions such as cloud fraction, should approximately cancel when comparing GOSAT and PHEOS-WCA.

Within the CO_2 assimilation community, there is an ongoing debate over the appropriate assimilation window length (i.e., the period of time for which the information from an observation is used to adjust the fluxes) including consideration of how the optimal window length is affected by the use of point measurements versus column data from ground-based remote sensing or satellites, and more detailed characteristics of the data density and coverage. Longer windows (1 or more years) are favored by some since a given measurement is considered to be impacted by fluxes over a long period, which is still much shorter than the lifetime of CO_2 in the atmosphere. Shorter windows (weeks or months) are favored by others, since fluxes closest in time and space to any point then have the largest impact on the CO_2 concentration and since the influence of fluxes farther in space/time is subject to larger transport errors.

In the present work, observations only constrain fluxes in the same month, which is not that different from the 5 week assimilation window of CarbonTracker [*Peters et al.*, 2007]. One can argue that since this is a relatively short

duration, it could give an advantage to HEO by omitting the constraints on Arctic and boreal fluxes from LEO observations farther away (northern temperate/tropical or Southern Hemisphere) for which the impacts of Arctic and boreal fluxes will not have had sufficient time to reach; however, any perturbations to these observations will be subject to larger transport errors. The monthly approach was actually chosen since an annual inversion, in which the seasonal cycle in the model was assumed to be correct, allowed HEO observations during the summer to constrain Arctic and boreal fluxes throughout the entire year, giving unrealistically large constraints (and unrealistically low uncertainties) on annual flux estimates.

In the inversion, we did not continually update the background CO_2 field over the course of the annual cycle; consequently, the influence of fluxes from earlier months is not completely mitigated in each monthly inversion. However, we believe that the impact of this on the monthly flux estimates is small because the high-density satellite observations provide a strong constraint on the fluxes in a given month. Furthermore, *Deng et al.* [2013] have shown that the CO_2 signal from fluxes in large regions such as Asia and Europe is well mixed into the background after about 2 months. In the context of the OSSE conducted here, we are able to recover the true fluxes, suggesting that the error incurred from our treatment of the effects of the fluxes from earlier months is indeed small. We do not expect that our results would differ significantly if a more sophisticated data assimilation approach were employed.

Regardless of the simplifying assumptions that were employed in our inversion approach, this work is a first quantitative look at the constraints on surface CO_2 fluxes from HEO and is only intended to be an initial look or first step. Given the nature of the continuous temporal viewing from HEO or GEO and the possibility of diurnal viewing of CO_2 with sensitivity in the planetary boundary layer, future work should investigate constraining fluxes at higher spatial and temporal scales and using more sophisticated data assimilation methods. In fact, the continuous observing capability throughout the daylight hours from HEO (or GEO) is arguably its most important observing characteristic, one which was barely exploited in our inversions. *Olsen and Randerson* [2004] model the XCO_2 diurnal cycle over Park Falls yielding an amplitude of ~1.0 ppm. *Keppel-Aleks et al.* [2012] show that the XCO_2 diurnal cycle in Total Carbon Column Observing Network measurements over Park Falls, Wisconsin is actually closer to 2.0 ppm. HEO XCO_2 observations spanning a large segment of the diurnal cycle could have sufficient precision for investigations into the diurnal variation of CO_2 fluxes in the Arctic and boreal regions.

In this work, we did not use the XCO_2 column averaging kernel, but rather used the XCO_2 averaging kernel matrix. Although these should be equivalent and using the matrix (instead of a vector) made many of the calculations more complicated, one reason for doing this was that as a future step, simulated NIR + TIR observations could be combined from PCW-PHEOS-WCA (and GOSAT) yielding vertical information about the CO_2 profile, which would provide additional constraints on surface CO_2 fluxes. Our use of the full averaging kernel matrix may facilitate better comparisons with the NIR + TIR OSSE.

Furthermore, although our focus in this work has been the investigation of constraints on biospheric CO_2 fluxes, a dense data set such as offered from HEO, may also enable the capability to constrain CO_2 emissions from northern high-latitude fossil fuel combustion, analogous to the findings of *Bovensmann et al.* [2010] for CarbonSat. As mentioned earlier, HEO satellites could be an important component of any future constellation of CO_2 satellites, providing high-latitude spatial coverage not obtained by GEO and temporal coverage not obtained from LEO. Additionally, in a constellation composed of three GEO satellites over North America, Europe, and East Asia, adding a HEO mission could provide midlatitude (~50–60°N) overlap with the GEO satellites that could help to detect any diurnally related biases between the GEO missions that might be missed with only a LEO Sun-synchronous satellite (and sparse ground-based column measurements) for comparison.

6. Conclusions

The OSSE described in this work demonstrates that NIR retrieved column-averaged CO_2 (XCO_2) from a HEO mission with characteristics consistent with the proposed PCW-PHEOS-WCA concept, offer improved constraints on Arctic and boreal biospheric CO_2 fluxes relative to a LEO mission with the capabilities of GOSAT. This is true in spite of the lower SNR for the proposed PCW-PHEOS-FTS (resulting from the smaller, lighter FTS design, and farther viewing distance) since the observing pattern results in a far greater number of observations during nonwinter months.

Two different instrument configurations for the PHEOS-WCA were compared along with scenarios including and excluding observations over snow. For Canada, Alaska, Scandinavia, Eastern Europe, and Siberia, the Optimal and

All-band (or Lite) configurations offered mean annual flux uncertainties of ~30% and ~20% lower than those from GOSAT, respectively, with little difference in the uncertainty ratios for different treatments of observations over snow. The flux uncertainty reduction from PHEOS observations for constraining summer Arctic and boreal fluxes is larger than the annual improvement, due to the seasonal pattern of observational coverage. Since the largest interannual flux variability and hence the largest uncertainty or bias in prior fluxes over Arctic and boreal regions occurs during the summer growing season, potential problems associated with the reduced winter observational coverage from a HEO mission are less severe than if flux uncertainties were uniformly distributed throughout the seasons. This increased summer observational capability would help to constrain fluxes related to changes in boreal and Arctic sources/sinks such as boreal forest disturbances or emission of CO_2 from Arctic permafrost thaw.

These findings demonstrate that CO_2 observations from HEO offer significant advantages over LEO for constraining CO_2 fluxes from the Arctic and boreal regions, even with conservative assumptions about the HEO mission's observing capabilities. However, the greatest benefit of the quasi-continuous observing capability from HEO or GEO may be the ability to measure throughout the daylight portion of the diurnal cycle, which was not well exploited in these inversions and could be better tested in higher temporal resolution OSSEs that investigate the constraints on the diurnal cycle offered by this approach. We hope to carry out such OSSEs in the future with a more sophisticated assimilation system that will also offer improved characterization of uncertainties.

Appendix A: Determination of Observation Coordinates for HEO Viewing

Determination of the longitude (λ) and latitude (ϕ) for HEO observations requires transforming the Cartesian *(x,y)* coordinates from the FOR using the inverse equations for an orthographic projection [*Snyder*, 1993], with respect to the origin of the projection located at the apogee (λ_0, ϕ_0).

$$\phi = \sin^{-1}\left[\cos c \sin\phi_0 + \frac{y \sin c \cos\phi_0}{\sqrt{x^2 + y^2}}\right] \tag{A1}$$

$$\lambda = \lambda_0 + \tan^{-1}\left[\frac{x \sin c}{\sqrt{x^2 + y^2} \cos\phi_0 \cos c - y \sin\phi_0 \sin c}\right] \tag{A2}$$

$$\text{where } c = \sin^{-1}\left[\frac{\sqrt{x^2 + y^2}}{R}\right] \tag{A3}$$

$R = 6371.0$ km (assuming a spherical Earth) and *(x,y)* are in kilometers relative to the apogee (x_0, y_0).

Also http://en.wikipedia.org/wiki/Orthographic_projection_(cartography).

Appendix B: Determination of Sunrise, Sunset, and Solar Zenith Angle

Sunrise and sunset were determined from the solar declination δ, which is a function of the day of year *J*:

$$\delta = 23.45° \sin\left(360° \frac{284 + J}{365}\right) \tag{B1}$$

From the declination, the day-length *D* in hours is [*Brock*, 1981; *Forsythe et al.*, 1995]:

$$D = 2 \frac{\cos^{-1}(A)}{15°} \quad \text{where } A = -\tan(\phi)\tan(\partial) \text{ and } -1 > A > 1 \tag{B2}$$

ϕ is the latitude. If $A > 1$, it is the polar night ($D = 0$ h) and if $A < -1$, it is the constant daylight ($D = 24$). Otherwise, the local times of sunrise and sunset (hour of day) are given by:

$$\text{Rise} = 12 - D/2, \text{Set} = 12 + D/2 \tag{B3}$$

The hour angle ω was also calculated since this parameter along with δ can be used to determine the solar zenith angle θ.

$$\omega = 15(t - 12) \text{ where } t \text{ is the local time in hours} \tag{B4}$$

$$\theta = \sin\delta \sin\phi + \cos\delta \cos\phi \cos\omega \tag{B5}$$

Approximations involved here include the assumption of a circular orbit for the Earth around the Sun, and sunrise/sunset defined as the point when the center of the Sun is even with the horizon. Although *Forsythe*

et al. [1995] state that the Center for Biosystems Modeling (CBM) model gives more accurate day-lengths than the *Brock* [1981] model when compared to the astronomical almanac, this fact only pertains to low latitude and midlatitude, with the accuracy of the CBM model degrading rapidly poleward of 60°; therefore, we use the simpler Brock model since the northern high latitudes are our primary region of interest.

References

Berk, A., G. P. Anderson, P. K. Acharya, and E. P. Shettle (2008), *MODTRAN® 5.2.0.0 User's Manual*, Spectral Sciences, Inc, Burlington, Mass.

Bernath, P. F., et al. (2005), Atmospheric Chemistry Experiment (ACE): Mission overview, *Geophys. Res. Lett.*, *32*, L15S01, doi:10.1029/2005GL022386.

Black, T. A., W. J. Chen, A. G. Barr, M. A. Arain, Z. Chen, Z. Nesic, E. H. Hogg, H. H. Neumann, and P. C. Yang (2000), Increased carbon sequestration by a boreal deciduous forest in years with a warm spring, *Geophys. Res. Lett.*, *27*(9), 1271–1274.

Boesch, H., D. Baker, B. Connor, D. Crisp, and C. Miller (2011), Global characterization of CO_2 column retrievals from shortwave-infrared satellite observations of the Orbiting Carbon Observatory-2 mission, *Remote Sens.*, *3*, 270–304, doi:10.3390/rs3020270.

Bovensmann, H., M. Buchwitz, J. P. Burrows, M. Reuter, T. Krings, K. Gerilowski, O. Schneising, J. Heymann, A. Tretner, and J. Erzinger (2010), A remote sensing technique for global monitoring of power plant CO_2 emissions from space and related applications, *Atmos. Meas. Tech.*, *3*, 781–811, doi:10.5194/amt-3-781-2010.

Bréon, F. M., D. M. O'Brien, and J. D. Spinhirne (2005), Scattering layer statistics from space borne GLAS observations, *Geophys. Res. Lett.*, *32*, L22802, doi:10.1029/2005GL023825.

Brock, T. D. (1981), Calculating solar radiation for ecological studies, *Ecol. Model.*, *14*, 1–19.

Brown, J., K. M. Hinkel, and F. E. Nelson (2000), The Circumpolar Active Layer Monitoring (CALM) program: Research designs and initial results, *Polar Geog.*, *24*(3), 165–258.

Burrows, J. P., et al. (2004), The geostationary tropospheric pollution explorer (GeoTROPE) mission: Objectives, requirements and mission concept, *Adv. Space Res.*, *34*, 682–687.

Butz, A., et al. (2011), Toward accurate CO_2 and CH_4 observations from GOSAT, *Geophys. Res. Lett.*, *38*, L14812, doi:10.1029/2011GL047888.

Cai, W.-J., et al. (2010), Decrease in the CO_2 uptake capacity in an ice-free Arctic Ocean Basin, *Science*, *329*, 556–559, doi:10.1126/science.1189338.

Chahine, M., C. Barnet, E. T. Olsen, L. Chen, and E. Maddy (2005), On the determination of atmospheric minor gases by the method of vanishing partial derivatives with application to CO_2, *Geophys. Res. Lett.*, *32*, L22803, doi:10.1029/2005GL024165.

Chahine, M. T., L. Chen, P. Dimotakis, X. Jiang, Q. B. Li, E. T. Olsen, T. Pagano, J. Randerson, and Y. L. Yung (2008), Satellite remote sounding of mid-tropospheric CO_2, *Geophys. Res. Lett.*, *35*, L17807, doi:10.1029/2008GL035022.

Chance, K., X. Liu, R. M. Suleiman, D. E. Flittner, and S. J. Janz (2012), Tropospheric Emissions: Monitoring of Pollution (TEMPO), Abstract A31B-0020 presented at 2012 Fall Meeting, AGU, San Francisco, Calif., 3–7 Dec.

Corbett, J. J., D. A. Lack, J. J. Winebrake, S. Harder, J. A. Silberman, and M. Gold (2010), Arctic shipping emissions inventories and future scenarios, *Atmos. Chem. Phys.*, *10*, 9689–9704, doi:10.5194/acp-10-9689-2010.

Crévoisier, C., A. Chédin, H. Matsueda, T. Machida, R. Armante, and N. A. Scott (2009), First year of upper tropospheric integrated content of CO_2 from IASI hyperspectral infrared observations, *Atmos. Chem. Phys.*, *9*, 4797–4810, doi:10.5194/acp-9-4797-2009.

Crisp, D., et al. (2004), The Orbiting Carbon Observatory (OCO) mission, *Adv. Space Res.*, *34*, 700–709.

Crisp, D., et al. (2012), The ACOS CO_2 retrieval algorithm—Part II: Global X_{CO_2} data characterization, *Atmos. Meas. Tech.*, *5*, 687–707, doi:10.5194/amt-5-687-2012.

Deng, F., et al. (2013), Inferring regional sources and sinks of atmospheric CO_2 from GOSAT XCO_2 data, *Atmos. Chem. Phys. Discuss.*, *13*, 26,327–26,388, doi:10.5194/acpd-13-26327-2013.

Derksen, C., and R. Brown (2012), Spring snow cover extent reductions in the 2008–2012 period exceeding climate model projections, *Geophys. Res. Lett.*, *39*, L19504, doi:10.1029/2012GL053387.

Fishman, J., et al. (2012), The United States' next generation of atmospheric composition and coastal ecosystem measurements. NASA's Geostationary Coastal and Air Pollution Events (GEO-CAPE) mission, *Bull. Am. Meteorol. Soc.*, *93*, 1547–1566, doi:10.1175/BAMS-D-11-00201.1.

Forsythe, W. C., E. J. Rykiel, R. S. Stahl, H. Wu, and R. M. Schoolfield (1995), A model comparison for daylength as a function of latitude and day of year, *Ecol. Model.*, *80*, 87–95.

Fu, D., K. Sung, C. D. Boone, K. A. Walker, and P. F. Bernath (2009), Ground-based solar absorption studies for the Carbon Cycle science by Fourier Transform Spectroscopy (CC-FTS) mission, *J. Quant. Spectrosc. Radiat. Transfer*, *109*, 2219–2243.

Gurney, K. R., et al. (2002), Towards robust regional estimates of CO_2 sources and sinks using atmospheric transport models, *Nature*, *415*, 626–630.

Halloran, P. R. (2012), Does atmospheric CO_2 seasonality play an important role in governing the air-sea flux of CO_2?, *Biogeosciences*, *9*, 2311–2323, doi:10.5194/bg-9-2311-2012.

Hansen, M., R. DeFries, J. R. G. Townshend, and R. Sohlberg (1998), *UMD Global Land Cover Classification, 1 Kilometer, 1.0*, pp. 1981–1994, Department of Geography, University of Maryland, College Park, Maryland.

Hansen, M., R. DeFries, J. R. G. Townshend, and R. Sohlberg (2000), Global land cover classification at 1 km resolution using a decision tree classifier, *Int. J. Remote Sens.*, *21*, 1331–1365.

Hansen, J., R. Ruedy, M. Sato, and K. Lo (2010), Global surface temperature change, *Rev. Geophys.*, *48*, RG4004, doi:10.1029/2010RG000345.

Japanese Aerospace Exploration Agency, National Institute for Environmental Studies, and Ministry of the Environment (2011), *GOSAT / IBUKI Data Users Handbook*, 1st ed., March 2011, Tsukuba, Japan.

Keeling, C. D. (1960), The concentration and isotopic abundance of carbon dioxide in the atmosphere, *Tellus*, *12*, 200–204.

Keppel-Aleks, G., et al. (2012), The imprint of surface fluxes and transport on variations in total column carbon dioxide, *Biogeosciences*, *9*, 875–891, doi:10.5194/bg-9-875-2012.

Kim, J., and the GEMS Team (2012), GEMS (Geostationary Environment Monitoring Spectrometer) onboard the GeoKOMPSAT to monitor air quality in high temporal and spatial resolution over Asia-Pacific Region, *Geophys. Res. Abstr.*, *14*, EGU2012 4051.

Kuang, Z., J. Margolis, G. Toon, D. Crisp, and Y. Yung (2002) Spaceborne measurements of atmospheric CO_2 by high-resolution NIR spectrometry of reflected sunlight: An introductory study, *Geophys. Res. Lett.*, *29*(15), 1716, doi:10.1029/2001GL014298.

Kulawik, S. S., et al. (2010), Characterization of Tropospheric Emission Spectrometer (TES) CO_2 for carbon cycle science, *Atmos. Chem. Phys.*, *10*, 5601–5603.

Kulawik, S. S., J. R. Worden, S. C. Wofsy, S. C. Biraud, R. Nassar, D. B. A. Jones, E. T. Olsen, G. B. Osterman, and the TES and HIPPO teams (2013), Comparison of improved Aura Tropospheric Emission Spectrometer (TES) CO_2 with HIPPO and SGP aircraft profile measurements, *Atmos. Chem. Phys.*, *13*, 3205–3225.

Kuze, A., H. Suto, M. Nakajima, and T. Hamazaki (2009), Thermal and near infrared sensor for carbon observation Fourier-transform spectrometer on the Greenhouse Gases Observing Satellite for greenhouse gases monitoring, *Appl. Opt.*, *48*(35), 6716–6733.

Lachance, R., et al. (2012), PCW/PHEOS-WCA: Quasi-geostationary Arctic measurements for weather, climate and air quality from highly eccentric orbits, in *Proc. SPIE*, Sensors, Systems, and Next-Generation Satellites XVI, vol. 8583, pp. 85330O-1, SPIE, Bellingham, WA, doi:10.1117/12.974795.

McConnell, J. C., et al. (2012), PCW/PHEOS-WCA: Quasi-geostationary viewing of the Arctic and Environs for weather, climate and air quality, Proc. of European Space Agency (ESA) Conference ATMOS 2012: Advances in Atmospheric Science and Applications, 2012 June 18–22, Bruges, Belgium.

McDonald, K. C., J. S. Kimball, E. Njoku, R. Zimmermann, and M. Zhao (2004), Variability in springtime thaw in the terrestrial high latitudes: Monitoring a major control on the biospheric assimilation of atmospheric CO_2 with spaceborne microwave remote sensing, *Earth Interact.*, *8*(20), 1–23.

McGuire, D., L. G. Anderson, T. R. Christensen, S. Dallimore, L. Guo, D. J. Hayes, M. Heimann, T. D. Lorenson, R. W. Macdonald, and N. Roulet (2009), Sensitivity of the carbon cycle in the Arctic to climate change, *Ecol. Monogr.*, *79*(4), 523–555.

Miller, C. E., and Dinardo, S. J. (2012), CARVE: The Carbon in Arctic Reservoirs Vulnerability Experiment, IEEE 2012 Aerospace Conference, pp. 1–17, doi:10.1109/AERO.2012.6187026.

Nassar, R., et al. (2010), Modeling global atmospheric CO_2 with improved emission inventories and CO_2 production from the oxidation of other carbon species, *Geosci. Model Dev.*, *3*, 689–716, doi:10.5194/gmd-3-689-2010.

Nassar, R., et al. (2011), Inverse modeling of CO_2 sources and sinks using satellite observations of CO_2 from TES and surface flask measurements, *Atmos. Chem. Phys.*, *11*, 6029–6047, doi:10.5194/acp-11-6029-2011.

O'Dell, C. W., et al. (2012), The ACOS CO_2 retrieval algorithm—Part 1: Description and validation against synthetic observations, *Atmos. Meas. Tech.*, *5*, 99–121, doi:10.5194/amt-5-99-2012.

Oechel, W. C., G. L. Vourlitis, S. J. Hastings, R. C. Zulueta, L. Hinzman, and D. Kane (2000), Acclimation of ecosystem CO_2 exchange in the Alaskan Arctic in response to decadal climate warming, *Nature*, *406*, 978–981.

Olsen, S. C., and J. T. Randerson (2004), Differences between surface and column atmospheric CO_2 and implications for carbon cycle research, *J. Geophys. Res.*, *109*, D02301, doi:10.1029/2003JD003968.

Peters, W. P., et al. (2007), An atmospheric perspective on North American carbon dioxide exchange: CarbonTracker, *Proc. Natl. Acad. Sci. U. S. A.*, *104*(48), 18,925–18,930.

Peters, G. P., T. B. Nilssen, L. Lindholt, M. S. Eide, S. Glomsrød, L. I. Eide, and J. S. Fuglestvedt (2011), Future emissions from petroleum and shipping activities in the Arctic, *Atmos. Chem. Phys.*, *11*, 5305, doi:10.5194/acp-11-5305-2011.

Reuter, M., et al. (2011), Retrieval of atmospheric CO_2 with enhanced accuracy and precision from SCIAMACHY: Validation with FTS measurements and comparison with model results, *J. Geophys. Res.*, *116*, D04301, doi:10.1029/2010JD015047.

Romanovsky, V. E., et al. (2011), Permafrost [in Arctic Report Card 2011]. [Available at http://www.arctic.noaa.gov/reportcard.]

Schaefer, K., T. Zhang, L. Bruhwiler, and A. P. Barrett (2011), Amount and timing of permafrost carbon release in response to climate warming, *Tellus B*, doi:10.1111/j.1600-0889.2011.00527.x.

Schneider von Deimling, T., M. Meinshausen, A. Levermann, V. Huber, K. Frieler, D. M. Lawrence, and V. Brovkin (2012), Estimating the near-surface permafrost-carbon feedback on global warming, *Biogeosciences*, *9*, 649–655.

Schneising, O., M. Buchwitz, M. Reuter, J. Heymann, H. Bovensmann, and J. P. Burrows (2011), Long-term analysis of carbon dioxide and methane column-averaged mole fractions retrieved from SCIAMACHY, *Atmos. Chem. Phys.*, *11*, 2863–2880, doi:10.5194/acp-11-2863-2011.

Schuur, E. A. G., et al. (2008), Vulnerability of permafrost carbon to climate change: Implications for the global carbon cycle, *BioScience*, *58*(8), 701–714.

Schwarz, J. P., R. S. Gao, A. E. Perring, J. R. Spackman, and D. W. Fahey (2013), Black carbon aerosol size in snow, *Sci. Rep.*, *3*, 1356, doi:10.1038/srep01356.

Snow, Water, Ice, and Permafrost in the Arctic (2011), Assessment: Executive summary, 16 pp., Arctic Monitoring and Assessment Program (AMAP) Secretariat, Oslo, Norway. [Available at www.amap.no.]

Snyder, J. P. (1993), *Flattening the Earth: Two Thousand Years of Map Projections*, Univ. of Chicago Press, Chicago and London, ISBN 0-226-76746-9.

Stinson, G., et al. (2011), An inventory-based analysis of Canada's managed forest carbon dynamics, 1990 to 2008, *Global Change Biol.*, *1–18*, 2227–2244, doi:10.1111/j.1365-2486.2010.02369.x.

Tarnocai, C., J. G. Canadell, E. A. G. Schuur, P. Kuhry, G. Mazhitova, and S. Zimov (2009), Soil organic carbon pools in the northern circumpolar permafrost region, *Global Biogeochem. Cycles*, *23*, GB2023, doi:10.1029/2008GB003327.

Trishchenko, A. P., and L. Garand (2011), Spatial and temporal sampling of polar regions from two-satellite system on Molniya orbit, *J. Atmos. Oceanic Technol.*, *28*, 977–992.

Trishchenko, A. P., L. Garand, and L. D. Trichtchenko (2011), Three-apogee 16-h highly elliptical orbit as optimal choice for continuous meteorological imaging of polar regions, *J. Atmos. Oceanic Technol.*, *28*, 1407–1422.

United Nations Environment Program (2012), Policy Implications of Warming Permafrost, (Nairobi, Kenya), ISBN: 978-92-807-3308-2, Job Number: DEW/1621/NA.

van der Werf, G. R., J. T. Randerson, L. Giglio, G. J. Collatz, M. Mu, P. S. Kasibhatla, D. C. Morton, R. S. DeFries, Y. Jin, and T. T. van Leeuwen (2010), Global fire emissions and the contribution of deforestation, savanna, forest, agricultural, and peat fires (1997–2009), *Atmos. Chem. Phys.*, *10*, 11,707–11,735, doi:10.5194/acp-10-11707-2010.

Velazco, V. A., M. Buchwitz, H. Bovensmann, M. Reuter, O. Schneising, J. Heymann, T. Krigs, K. Gerilowski, and J. P. Burrows (2011), Towards space based verification of CO_2 emissions from strong localized sources: Fossil fuel power plant emissions as seen by a CarbonSat constellation, *Atmos. Meas. Tech.*, *4*, 2809–2822.

Wang, M., and J. E. Overland (2012), A sea ice free summer Arctic within 30 years: An update from CMIP5 models, *Geophys. Res. Lett.*, *39*, L18501, doi:10.1029/2012GL052868.

World Meteorological Organization (2009), Vision for the GOS in 2025, Proc. Ninth Consultative Meeting on High-Level Policy on Satellite Matters, Port of Spain, Trinidad and Tobago, World Meteorological Organization, 19 pp.

Wunch, D., et al. (2011), A method for evaluating bias in global measurements of CO_2 total columns from space, *Atmos. Chem. Phys.*, *11*, 12,317–12,337, doi:10.5194/acp-11-12317-2011.

Xu, L., et al. (2013), Temperature and vegetation seasonality diminishment over northern lands, *Nat. Clim. Change*, *3*, doi:10.1038/nclimate1836.

Yokota, T., Y. Yoshida, N. Eguchi, Y. Ota, T. Tanaka, H. Watanabe, and S. Maksyutov (2009), Global concentrations of CO_2 and CH_4 retrieved from GOSAT: First preliminary results, *Sci. Online Lett. Atmos. (SOLA)*, *5*, 160–163, doi:10.2151/sola.2009-041.

Yoshida, Y., Y. Ota, N. Eguchi, N. Kikuchi, K. Nobuta, H. Tran, I. Morino, and T. Yokota (2011), Retrieval algorithm for CO_2 and CH_4 column abundances from short-wavelength infrared spectral observations by the Greenhouse gases observing satellite, *Atmos. Meas. Tech.*, *4*, 171–734, doi:10.5194/amt-4-717-2011.

Yoshida, Y., et al. (2013), Improvement of the retrieval algorithm for GOSAT SWIR XCO2 and XCH4 and their validation using TCCON data, *Atmos. Meas. Tech.*, *6*, 1533–1547, doi:10.5194/amt-6-1533-2013.